Personalized Medicine and Imaging

Clinical Cancer Research

Voxel Level Radiologic–Pathologic Validation of Restriction Spectrum Imaging Cellularity Index with Gleason Grade in Prostate Cancer

Ghiam Yamin[1], Natalie M. Schenker-Ahmed[1], Ahmed Shabaik[2], Dennis Adams[2], Hauke Bartsch[1], Joshua Kuperman[1], Nathan S. White[1], Rebecca A. Rakow-Penner[1], Kevin McCammack[1], J. Kellogg Parsons[3], Christopher J. Kane[3], Anders M. Dale[1,4], and David S. Karow[1]

Abstract

Purpose: Restriction spectrum imaging (RSI-MRI), an advanced diffusion imaging technique, can potentially circumvent current limitations in tumor conspicuity, *in vivo* characterization, and location demonstrated by multiparametric magnetic resonance imaging (MP-MRI) techniques in prostate cancer detection. Prior reports show that the quantitative signal derived from RSI-MRI, the cellularity index, is associated with aggressive prostate cancer as measured by Gleason grade (GG). We evaluated the reliability of RSI-MRI to predict variance with GG at the voxel-level within clinically demarcated prostate cancer regions.

Experimental Design: Ten cases were processed using whole mount sectioning after radical prostatectomy. Regions of tumor were identified by an uropathologist. Stained prostate sections were scanned at high resolution (75 μm/pixel). A grid of tiles corresponding to voxel dimensions was graded using the GG system. RSI-MRI cellularity index was calculated from presurgical prostate MR scans and presented as normalized *z*-score maps. In total, 2,795 tiles were analyzed and compared with RSI-MRI cellularity.

Results: RSI-MRI cellularity index was found to distinguish between prostate cancer and benign tumor ($t = 25.48$, $P < 0.00001$). Significant differences were also found between benign tissue and prostate cancer classified as low-grade (GG = 3; $t = 11.56$, $P < 0.001$) or high-grade (GG $\geq$ 4; $t = 24.03$, $P < 0.001$). Furthermore, RSI-MRI differentiated between low and high-grade prostate cancer ($t = 3.23$; $P = 0.003$).

Conclusions: Building on our previous findings of correlation between GG and the RSI-MRI among whole tumors, our current study reveals a similar correlation at voxel resolution within tumors. Because it can detect variations in tumor grade with voxel-level precision, RSI-MRI may become an option for planning targeted procedures where identifying the area with the most aggressive disease is important. *Clin Cancer Res; 22(11); 2668–74. ©2016 AACR.*

Introduction

Prostate cancer is the most common noncutaneous cancer and the second leading cause of cancer-related death in U.S. men (1). Most prostate cancers are adenocarcinomas (95%) that develop from prostatic gland secretory luminal cells; approximately 70% arise in the peripheral zone (2, 3), approximately 20%–25% arise in the transition zone (3, 4), and approximately 8% arise in the central zone (3).Randomized trials have confirmed the efficacy of prostate-specific antigen (PSA) population screening to diminish prostate cancer mortality (5). However, aggressive population screening with PSA increases the detection of both lethal and nonlethal cancers, which can promote overdetection and overtreatment of nonlethal cancers. Decreasing prostate cancer mortality, while minimizing the potential morbidities of overdetection and overtreatment, requires refined approaches to screening and diagnosis using novel, noninvasive biomarkers to differentiate indolent from clinically significant disease.

Multiparametric magnetic resonance imaging (MP-MRI) is a rapidly evolving noninvasive diagnostic tool that has been used to complement other emerging biomarkers in the screening, staging, monitoring, and treatment of prostate cancer (6). However, prostate MRI is confounded by variable sensitivity (36%–100%) and specificity (64%–95%), which curtails its clinical utility (7, 8). Diffusion weighted imaging (DWI), an advanced MRI modality, detects the impeded diffusivity of water in the intra- and extracellular compartments and has shown correlation with prostate cancer. However, DWI is limited by magnetic field inhomogeneity and high false-positive rates from inflammation, hemorrhage, or benign nodules in the transitional zone, which limit tumor conspicuity and location (9).

Restriction spectrum imaging (RSI-MRI) is an advanced imaging technique that shows improved conspicuity and differentiation of solid tumors compared with traditional

[1]Department of Radiology, University of California San Diego School of Medicine, San Diego, California. [2]Department of Pathology, University of California San Diego School of Medicine, San Diego, California. [3]Department of Surgery, University of California San Diego School of Medicine, San Diego, California. [4]Department of Neurosciences, University of California, San Diego, La Jolla, California.

Note: Supplementary data for this article are available at Clinical Cancer Research Online (http://clincancerres.aacrjournals.org/).

G. Yamin and N.M. Schenker-Ahmed contributed equally to this article.

Corresponding Author: David S. Karow, University of California, San Diego, 200 W Arbor Dr, #8756, San Diego, CA 92103. Phone: 619-543-3534; Fax: 619-543-3746; E-mail: dkarow@ucsd.edu

doi: 10.1158/1078-0432.CCR-15-2429

©2016 American Association for Cancer Research.

Downloaded from clincancerres.aacrjournals.org on October 19, 2021. © 2016 American Association for Cancer Research.

Translational Relevance

Current multiparametric magnetic resonance imaging (MP-MRI) techniques for detecting prostate cancer are limited with respect to tumor conspicuity assessment, *in vivo* characterization, and localization. We have demonstrated that a novel diffusion-based MRI technique, restriction spectrum imaging (RSI-MRI), differentiates among benign, low-grade, and high-grade prostate cancer at a voxel-level resolution. Use of an RSI-MRI index to differentiate between clinically relevant low- and high-grade categories of tumor prostate cancer aggressiveness may help improve and refine diagnosis and staging of prostate cancer. In addition, because it can detect intratumor variation, RSI-MRI may have particular relevance for the planning targeted therapies such as radiation seed therapy placement, magnetic resonance (MR)-guided focused ultrasound surgery, and MR-guided targeted biopsy.

DWI methods (10, 11). The RSI-MRI method can differentiate hindered versus restricted diffusion, thought to correspond to the extracellular and intracellular water compartments, respectively (12). RSI-MRI demonstrates improved signal-to-noise in tumor detection and exhibits reduced spatial distortion. We previously reported that the RSI-MRI cellularity index is associated with the detection of aggressive prostate cancer as defined by GG (13), and RSI-MRI provides improved sensitivity in the detection of extraprostatic extension of prostate cancer compared with standard MRI (14). To account for tumor grade heterogeneity within and between tumors, we sought to analyze histopathologic whole mount (WM) prostate cancer section at the voxel level. We hypothesized that pathology grading at this level of resolution would provide a more accurate representation of the intratumor variability that may be masked within an overall grade assigned to large tumor regions of interest (ROI). Here, we report the correlation of voxel-level Gleason graded prostate cancer specimens with RSI-MRI and discuss possible diagnostic and prognostic information gained from such analyses.

Materials and Methods

RSI

All patients in this Institutional review board–approved study were previously diagnosed with prostate cancer status after ultrasound-guided transrectal biopsy. Prior to radical prostatectomy, a pelvic MRI was performed to aid in surgical planning. Patients were scanned using a 3.0-T SignaHDxt MRI Scanner (General Electric) and a cardiac coil; no endorectal coil was used. The entire prostate was imaged, with axial slices oriented perpendicular to the rectal wall. T2-weighted images were acquired using a fast spin echo protocol with 3.0 mm contiguous slices. The RSI-MRI protocol parameters included *b*-values of 0, 125 (6 unique directions), 375 (6 unique directions), and 1,000 (15 unique directions) s/mm^2. The RSI-MRI protocol increased the total duration of the MRI scan time by 5 minutes. Additional details of the pulse sequence parameters can be found in Supplementary Table S1. RSI-MRI maps were reconstructed on the basis of all *b*-values and standardized across the sample to produce the *z*-score cellularity map. Specifically, *z*-score cellularity maps were produced using mean and SDs of normal prostate signal from the raw RSI-MRI maps in the benign tissue in the patient population, subtracting the mean value from an individual subjects' RSI-MRI cellularity map, and dividing by the benign prostate SD. Corrections for spatial distortion due magnetic field inhomogeneity in echo planar imaging were accomplished with an alternating phase-encode technique (15). After correction for spatial distortion, RSI-MRI maps were coregistered to the T2 images.

Digital histopathology and scoring

In general, the radical prostatectomy cases were consecutive surgeries; however, some cases were excluded because of significant artifacts in the histology, which would have made coregistration nearly impossible. Status post–radical prostatectomy, WM histopathology was performed on 5-μm thick sections. Each hematoxylin and eosin (H&E)-stained histopathologic section was reviewed by a board-certified surgical pathologist (A. Shabaik), who demarcated ROIs corresponding to tumor. The H&E digital images were acquired with a Keyence BZ-X710 All-in-one fluorescence microscope (Osaka) using transmitted light with a CFI Plan Apo λ 10× objective lens. To image the entire tissue section, the perimeter of the stained tissue was marked using low magnification (2×), and then automatically acquired with the 10× objective. The microscope automatically focused each image tile of the mosaic. Exposure time and white balance were calculated automatically by the system. All scans were acquired at high resolution (0.75488 μm/pixel). Tiles representing the entire image were then reconstructed into a "digital prostate map" interface and tumor ROIs overlaid with an alphanumeric grid containing tiles corresponding to voxel dimensions as shown in Fig. 1 and 2.

GG is the gold standard for grading prostate cancer aggressiveness (16–18), and is used to categorize prostate tissue based on histologic patterns. Tissue is given a grade from 1–5, with larger numbers typically indicating more aggressive cancer, characterized by poorly differentiated tissue, and, generally, a worse prognosis. Each tile in the overlaid alphanumeric grid was assessed for primary GG. Scoring for the current study focused on the primary grade that covered greater than 51% of the tile area, despite presence of other secondary grades that were higher or lower. For example, if 60% of the tile represented GG 4 but the rest was GG 5 (traditionally assigned a 4 + 5 Gleason score pattern), the final GG used for that tile in this study would be GG 4. Following current practice, only tiles with tissue of grades 3–5 were assigned a score; other tiles were scored as benign. A score of 0 was used to represent a benign area. Scored digital tiles were reviewed for accuracy by the same uropathologist who reviewed the H&E-stained histopathologic slide. A recent similarly conceptualized scoring framework, based on a five-grade group system founded on Gleason score, has shown improved risk stratification compared with the modern Gleason scoring system (17).

Registration of RSI-MRI with histopathology

A radiologist with experience in prostate cancer MR imaging (D.S. Karow) selected the slice from the T2 MRI series that corresponded most closely to the plane of the histopathology section. To correct for deformation of the 2D slice that may have occurred during histologic processing, the Control Point Selection Tool in MATLAB (Release 2010b. The MathWorks,

Downloaded from clincancerres.aacrjournals.org on October 19, 2021. © 2016 American Association for Cancer Research.

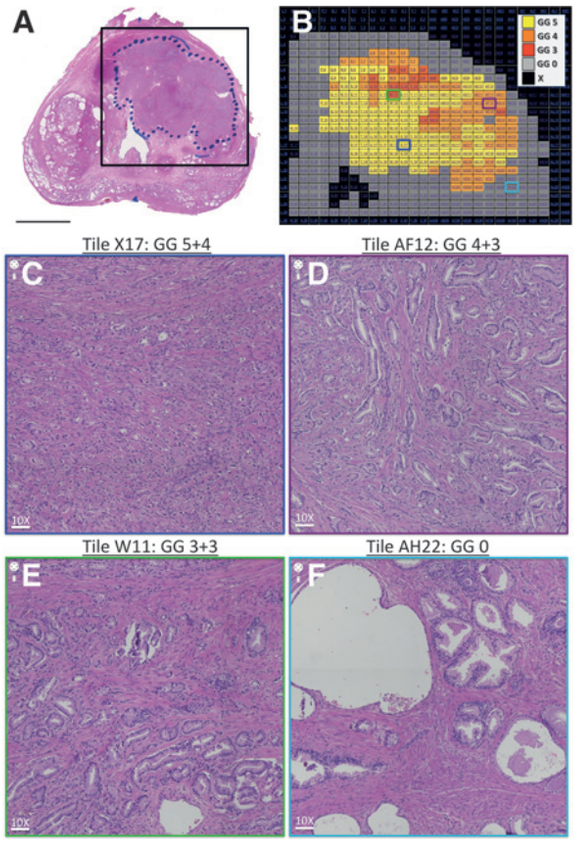

Figure 1.
"Digital prostate map" histopathologic section and example grid overlay. A, H&E-stained WM histopathologic prostate with a black box surrounding tumor ROI that represents the boundaries of a grid for sectioning the tumor area into voxel-sized tiles for grading purposes. Scale bar, 1 cm. B, H&E-stained WM histopathologic prostate section reconstructed into a "digital prostate map" interface online. Alphanumeric grid represents the outlined box in A surrounding the tumor ROI. Gleason grade is coded by color as defined by the key. C, representative tile (X17), showing Gleason grade 5+4 = 9 tumor architecture at 10× magnification. Scale bar, 75.5 μm. D, representative tile (AF12) showing Gleason grade 4+3 = 7 tumor architecture at 10× magnification. Scale bar, 75.5 μm. E, representative tile (W11), showing Gleason grade 3+3 = 6 tumor architecture at 10× magnification. Scale bar, 75.5 μm. F, representative tile (AH22), showing benign architecture at 10× magnification. Scale bar, 75.5 μm.

Inc.) was used to affine transform the selected T2 MRI slice to the shape and dimension of the histopathology section. The same transformation was applied to the registered RSI-MRI cellularity maps (Fig. 2). Anatomical landmarks, including the prostate shape, position of the urethra, and prominent benign prostatic hyperplasia nodules, were used to align the T2 MRI image as much as possible to the whole-mount sections. The Euclidean distance between transformed points and target points was calculated. The average registration error across all 10 subjects was 1.84 μm.

Statistical analysis

Linear mixed-effect with a random effect (19) of subject was used to determine the effectiveness of RSI-MRI in detecting tumor aggressiveness, by comparing benign tissue to increasingly aggressive tissue [benign vs. low-grade prostate cancer (Gleason 3) vs. high-grade prostate cancer (Gleason 4 and Gleason 5)]. *Post hoc* multiple comparison *t* tests (20) were used to assess RSI-MRI's ability to differentiate between normal prostate tissue and different levels of tumor aggressiveness (benign vs. low-grade prostate cancer and benign vs. high-grade prostate cancer) and between tumor grades (low-grade prostate cancer vs. high-grade prostate cancer). Statistical significance, $P < 0.05$, was determined using the software program R (21). The data were then plotted using SigmaPlot 12.5 (Systat Software Inc.).

Results

Ten patients, representing a range of tumor aggressiveness, who were evaluated with a preoperative MRI and RSI-MRI underwent radical prostatectomy and underwent surgery between March 2014 to December 2014 with WM specimens (Table 1). T2-weighted MRI images and RSI-MRI cellularity maps were coregistered with the WM prostate histopathologic section as depicted in four cases (Fig. 2). The 10 WM prostate cancer cases encompassed 17 tumor ROIs. Two patients had two distinct tumor ROIs, one patient had three distinct tumors ROIs, and another patient had four distinct tumor ROIs within one specimen. All patients with ≤2 ROIs had concordant tumors. Tumor ROIs were overlaid with an alphanumerical grid (Fig. 1), with the size of each square of the grid corresponding to the voxel dimensions used for acquisition of the RSI-MRI. We analyzed 2,795 total squares of WM prostate H&E-stained sections, of which 1,573 and 1,222 (Gleason 3: 267; Gleason 4: 392; Gleason 5: 563) comprised benign and tumor tissue, respectively.

RSI-MRI data for both normal and tumor regions were normally distributed. The mean cellularity index in prostate cancer was 1.81 (SEM = 0.05) and in benign tissue was −0.32 (SEM = 0.03). A linear mixed-effect with a random effect (19) of subject was employed to determine the association of RSI-MRI cellularity index with prostate cancer (benign vs. low-grade prostate cancer vs. high-grade prostate cancer; Table 2). RSI-MRI cellularity index distinguished benign from increasingly malignant prostate cancer ($P < 1\times10^{-5}$; Table 2). Both low- and high-grade prostate cancer showed significant differences in RSI-MRI signal compared with benign tissue (both $P < 0.001$; Table 3). Furthermore, significant difference in the RSI-MRI signal between pathologic categories, namely between low- and high-grade prostate cancer, was observed ($P = 0.003$; Table 3). Of note, we observed a trend of higher mean RSI-MRI cellularity with increasing grade (Gleason 3–5) versus benign tissue (Fig. 3). By leaving out either individual voxels or individual subjects, we conducted leave-one-out analyses, and in each case recalculated the model and predicted the left out RSI-MRI values using the new model. The resulting root mean squared errors from this analysis were 1.425 and 1.618 for leaving out voxels and subjects, respectively.

Discussion

We analyzed voxel-level Gleason-graded histopathologic samples in comparison with RSI-MRI cellularity indices obtained from presurgical *in vivo* MR scans. The data from the current study build on our previous findings of correlation between GG and the RSI-MRI cellularity index at the tumor

Downloaded from clincancerres.aacrjournals.org on October 19, 2021. © 2016 American Association for Cancer Research.

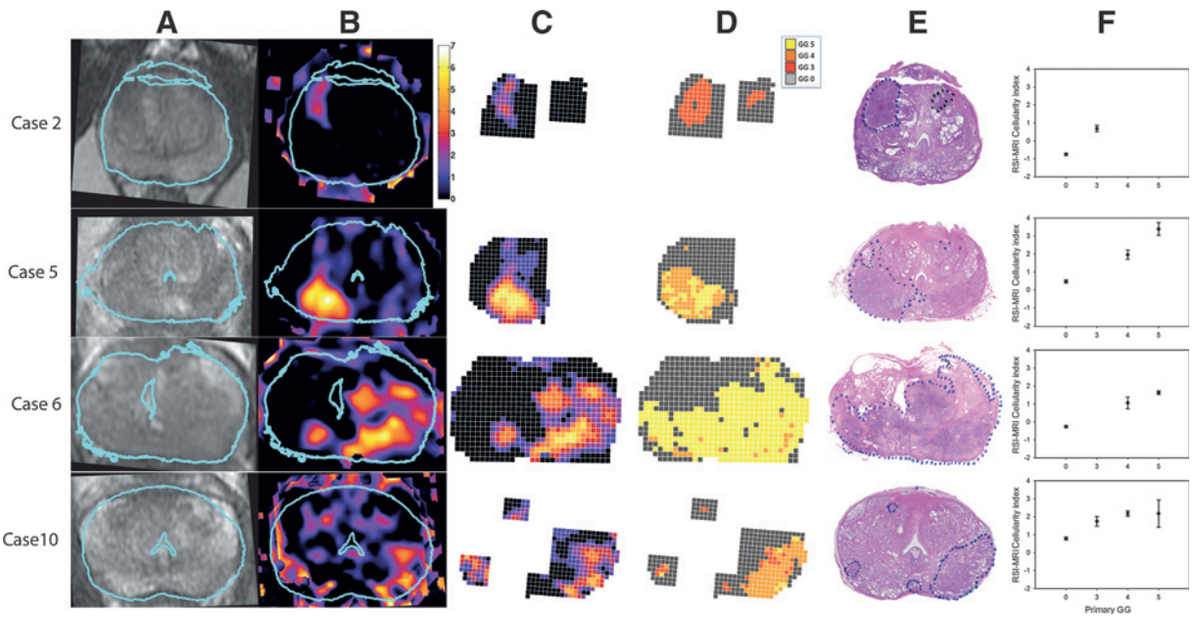

Figure 2.
T2, RSI-MRI, GG, and H&E: Cases 2, 5, 6, and 10. A, T2-weighted MR images, after in-plane affine transformation to correspond to the histopathology slides, RSI-MRI color coded cellularity maps (B), "Digital prostate map" grid overlay color-coded for RSI-MRI cellularity index (C), "Digital prostate map" grid overlay color-coded for Gleason grade (D), H&E-stained WM histopathologic prostate section with tumor area(s) outlined (E), plots for each case of the mean RSI-MRI signal corresponding to each histologic GG based on voxel-level analysis (F). Error bars, SEM. Blue outline in A and B indicates the correspondence of the histopathology slide to the MR image.

level in a sample that included the 10 patients in the current study (22) and reveal a correlation between the same parameters at the voxel level, demonstrating the ability of the RSI-MRI cellularity index to detect variation of GG within a single tumor.

MP-MRI is currently regarded as the standard-of-care noninvasive imaging biomarker for diagnosing and staging prostate cancer, despite its variable reliability in providing accurate diagnosis. The RSI-MRI method overcomes the limitations of DWI in MP-MRI by minimizing the extracellular diffusivity (or hindered component) seen in conventional DWI and capitalizing on the intracellular signal diffusivity (or restricted component) to detect regions of high cellularity, which can be associated with increased tumor burden (13, 14). RSI-MRI presents several advancements to currently implemented MP-MRI tumor imaging, including improved signal-to-noise in tumor detection and reduced spatial distortion.

RSI-MRI is designed to optimize the signal from the restricted intracellular water compartment, which is increased in tumor cells (12). Although GG is not a direct measure of cellularity, it is qualitatively based on architectural features that may indirectly relate to cellularity. Therefore, we expect the RSI-MRI cellularity index to correlate with tumor aggressiveness as measured by pathologic grade or GG. Novel to the traditional method of Gleason reporting and its application to radiologic–pathologic correlation with RSI-MRI, is our use of WM histopathologic sections scored at the voxel level. Traditionally, the pathologist highlights a tumor ROI and reports a general score for that area. In fact, this methodological approach was used recently to demonstrate that RSI-MRI detects increasingly aggressive prostate cancer, as defined by Gleason scores (13). We performed voxel-level pathologic grading with the rationale that pathologic assessment at this level of resolution is a more accurate representation of tumor variability. It is possible that the heterogeneity of different tumor grades may be masked within an overall grade assigned to large tumor ROIs.

Our previous studies (13, 22) have demonstrated the ability of RSI-MRI to discriminate among different grades of prostate cancer on a tumor-by-tumor basis. This study takes those findings to a resolution that is at least two orders of magnitude higher. Instead of analyzing each tumor as a whole, we analyzed each tumor at the level of the RSI-MRI voxel resulting in hundreds of samples per subject. This enabled us to investigate the ability of RSI-MRI to detect pathologic variation within tumors. In concordance with our prior radiologic–pathologic correlation performed on ROIs (13), the data in the current study demonstrate that the RSI-MRI cellularity index distinguishes between prostate cancer aggressiveness within tumors' GG at the voxel level.

The ability of RSI-MRI to differentiate tumor aggressiveness (low-grade vs. high grade) could have clinical implications in regards to prostate cancer management and treatment. Patients with low-grade disease are candidates for active surveillance. In contrast, patients with high-grade disease are subject to more aggressive treatment (radiation, surgery, and/or hormonal therapy; ref. 6). The goal of active surveillance is to detect aggressive forms of prostate cancer that have metastatic potential while actively monitoring indolent tumors. Knowledge of pathologic progression during monitoring, aided by a noninvasive method, could improve our management decisions in determining treatment. In this regard, serial imaging with RSI-MRI may afford the clinician an opportunity to monitor disease progression and assist in determining when biopsy is necessary. Furthermore, the ability of RSI-MRI to detect within tumor variability has implications for

Downloaded from clincancerres.aacrjournals.org on October 19, 2021. © 2016 American Association for Cancer Research.

Table 1. Demographics of 10 patients who had a preoperative MRI with subsequent radical prostatectomy

Case	Race	Age	PSA	Clinical stage	Location of positive biopsy[a]	Biopsy grade	Days between biopsy and MRI	Positive cores	Tumor volume (%)	WM Grade	Pathologic stage
1	White	61	9.8	T1c	L. Lateral Base	3+4	553	2 of 12	1.3	3+4[b]	pT2cNX
					L. Medial Base	3+3					
2	White	58	5.7	T2a	R. Mid	3+4	314	3 of 12	9	3+3[b]	pT2cN0
					L. Lateral Base	3+4					
					L. Apex	3+4					
3	White	68	4.7	T1c	L. Lateral Base	3+4	65	2 of 12	2.9	4+3	pT2aN0
					L. Lateral Mid	3+4					
4	White	73	6.2	T1c	L. Apex	3+4	97	3 of 19	12.6	5+3	pT2cN0
					L. Lateral Mid	3+3					
					R. Lateral Mid	3+3					
5	White	69	7.4	T2c	R. Lateral Apex[c]		33	7 of 12	18	4+5[d]	pT3aN0
					R. Lateral Mid[c]	5+4			0.8	4+5[e]	
					R. Lateral Base[c]	3+5			0.28	3+3[e]	
					R. Medial Base[c]						
					L. Lateral Mid[f]	5+4					
					L. Lateral Base	5+5					
					L. Medial Mid[f]						
6	White	54	16.7	T2c	R. Lateral Base	4+5	26	9 of 14	60–70	5+4	pT3bN1
					R. Medial Base	5+5					
					R. Medial Mid	5+5					
					L. Lateral Apex	5+4					
					L. Lateral Mid	5+4					
					L. Lateral Base	5+4					
					L. Medial Base	5+5					
					L. Medial Mid	5+5					
					L. Transi. Zone	5+5					
7	White	68	21.5	T1c	R. Medial Apex[g]	4+3	33	5 of 17	26	4+4	pT3aN0
8	White	66	1.05	T2a	R. Lateral Mid	3+3	61	1 of 12	5.3	3+4	pT2cNX
									1	3+3[h]	
9	White	63	9.4	T1c	Not specified	3+3	127	2 of 7	<2	4+3[i]	pT2cNX
10	African American	51	9.3	T1c	L. Lateral Mid	3+4	85	2 of 14	4.4	4+3[j]	pT2cN0
					L. Lateral Apex	3+4			<1	3+3[k]	

Abbreviations: L., Left; Med., Medial; MRI, magnetic resonance imaging; PSA, prostate serum antigen; R., Right; WM, whole mount.
[a]Standard 12-core biopsies.
[b]Additional outlined tumors of concurrent grade marked by pathologist.
[c]Intraductal carcinoma.
[d]Dominant tumor in R. apex to base.
[e]Additional tumors in L. Base and L. Apex.
[f]High-grade prostatic intraepithelial neoplasia.
[g]Five of six cores for the R. Medial Apex were contained adenocarcinoma.
[h]Scattered microscopic foci.
[i]Two additional microscopic foci present.
[j]Dominant tumor in L. mid lateral with additional outlined tumors of concurrent grade in the R. mid prostate, R. apex, and L. base.
[k]Multiple microscopic foci.

targeted treatments or procedures, such as MRI-guided fusion biopsies. With this novel technology, such biopsies would be better able to target the foci that contain the highest grade of disease. Similarly, evolving image-guided focal therapies could conceivably target the area of the highest grade disease with voxel-level precision.

Limitations of our study include a restricted patient sample pool (10 patients). However, this is mitigated by the large sample

Table 2. Voxel level statistical analysis of RSI-MRI cellularity index versus benign or malignant tissue in histopathological section (GGs 3–5). A linear mixed-effects model with a random effect of subject was implemented to compare difference in detection among benign tissue versus low-grade prostate cancer (primary Gleason 3) versus high-grade prostate cancer (primary Gleason $\geq$4)

Random effects: Subject

	Intercept	Residual
SD	0.7444	1.423

Fixed effects: RSI-MRI cellularity index vs. prostate cancer tumor grade

	Value	SE	DF	*t* value	*P*
(Intercept)	0.1589	0.2386	2783	0.6660	0.5055
Low-grade	1.153	0.0998	2783	11.56	$<1\times10^{-5}$
High-grade	1.516	0.0631	2783	24.03	$<1\times10^{-5}$

Abbreviation: DF, degrees of freedom.

Downloaded from clincancerres.aacrjournals.org on October 19, 2021. © 2016 American Association for Cancer Research.

Table 3. Voxel level statistical comparing RSI-MRI cellularity index between prostate cancer Gleason categories versus normal tissues and between pathologic grades. *Post hoc* multiple comparison *t* tests were implemented in comparing difference in detection of prostate cancer aggressiveness [low-grade prostate cancer (primary Gleason 3) and high-grade prostate cancer (primary Gleason ≥4)] versus benign tissue and between tumor grades (low-grade prostate cancer versus high-grade prostate cancer)

Group		Mean difference (SE)	*P*
Pathology vs. normal			
	Low grade vs. normal	1.153 (0.100)	<0.001
	High grade vs. normal	1.516 (0.063)	<0.001
Between pathologic grades			
	High grade vs. low grade	0.364 (0.113)	0.003

size (>2,700) of our voxel-based analysis, which is a novel approach that is not previously reported elsewhere. Other possible limitations include potential signal coregistration artifacts by tumor burden adjacent to the prostate boundary. Further limitations include lack of secondary pathologic characteristic by not accounting for areas of primary score versus secondary score. Truly heterogeneous tumors that exhibit intermixing of different GGs can confound simple grading criteria, especially if tumor characteristics represent a hybrid of ≥2 different grades. We contend that secondary pathologic characteristics are less likely when examining the histopathology at voxel-level accuracy versus whole tumors.

Moreover, because GG does not directly represent cellularity, it may not be the most effective measure for understanding how RSI-MRI reflects tissue components. For instance, we expect that RSI-MRI will have lesser ability to detect low-grade disease (GG ≤ 3); however, in certain cases (e.g. Fig. 2, Case 2), we find that the RSI-MRI signal is greater within the tumor than we would expect. In such cases, quantitative analysis of tissue compartments, such as the glandular structure and cell number and density, may yield a greater understanding of the nature of the RSI-MRI signal. Future studies are planned to determine the relationship of RSI-MRI to quantitative tumor cellular characteristics, including extracellular, intracellular, and intranuclear compartments.

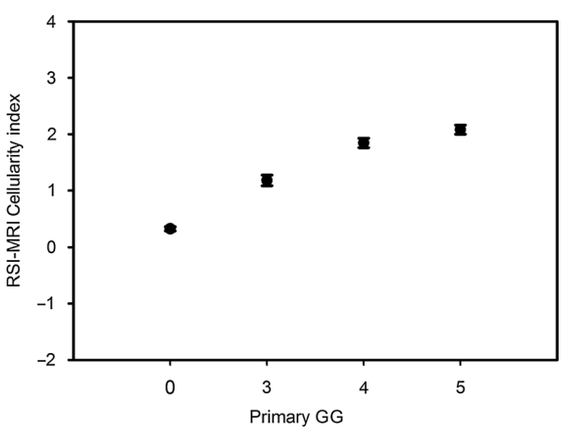

Figure 3.
RSI-MRI mean cellularity index grouped by pathologic Gleason grade. Mean RSI-MRI cellularity index represented as a *z*-score corresponding to histologic Gleason grade using data from all voxels graded in all cases. Error bars, SEM.

Another interesting question not addressed in this study is the issue of variation between different zones within the prostate that is apparent in both MRI and in histology. (23, 24) We have not yet investigated the variability of RSI-MRI signal among tumors in different regions. Future studies investigating this issue will require more cases with tumor burden in a wide variety of locations to answer this question.

Conclusions

Building on our previous findings of correlation between GG and the RSI-MRI among whole tumors, our current study reveals a similar correlation at voxel resolution within tumors. The relationship between GG and RSI-MRI suggests that RSI-MRI may be used as a component of active surveillance to noninvasively detect high-grade cancer and affect staging and treatment. Furthermore, because it can detect variations in tumor grade with voxel-level precision, RSI-MRI may be a promising option for planning of focal procedures, such as MRI-guided targeted biopsies and targeted radiotherapy, where identifying the area with the most aggressive disease is particularly important.

Disclosure of Potential Conflicts of Interest

A. Dale has ownership interest (including patents) in and is a consultant/advisory board member for Human Longevity, Inc. and CorTechs Labs, Inc., and reports receiving commercial research grants from General Electric Healthcare. No potential conflicts of interest were disclosed by the other authors.

Authors' Contributions

Conception and design: G. Yamin, N.M. Schenker-Ahmed, J. Kuperman, N.S. White, R. Rakow-Penner, K.C. McCammack, J.K. Parsons, A. Dale, D.S. Karow

Development of methodology: G. Yamin, N.M. Schenker-Ahmed, H. Bartsch, J. Kuperman, K.C. McCammack, A. Dale, D.S. Karow

Acquisition of data (provided animals, acquired and managed patients, provided facilities, etc.): G. Yamin, N.M. Schenker-Ahmed, D. Adams, J. Kuperman, C.J. Kane, A. Dale, D.S. Karow

Analysis and interpretation of data (e.g., statistical analysis, biostatistics, computational analysis): G. Yamin, N.M. Schenker-Ahmed, A. Shabaik, D. Adams, J. Kuperman, N.S. White, A. Dale, D.S. Karow

Writing, review, and/or revision of the manuscript: G. Yamin, N.M. Schenker-Ahmed, A. Shabaik, D. Adams, J. Kuperman, R. Rakow-Penner, K.C. McCammack, J.K. Parsons, C.J. Kane, A. Dale, D.S. Karow

Administrative, technical, or material support (i.e., reporting or organizing data, constructing databases): G. Yamin, N.M. Schenker-Ahmed, D. Adams, H. Bartsch, J. Kuperman, A. Dale, D.S. Karow

Study supervision: G. Yamin, A. Shabaik, A. Dale, D.S. Karow

Grant Support

This work was supported by the Department of Defense (DoD) grant, Prostate Cancer Research Program (#W81XWH-13-1-0391), the American Cancer Society Institutional Research grant (#70-002), UCSD Clinician Scientist Program (#5T32EB005970-07), UCSD School of Medicine Microscopy Core and NINDS P30 core grant (#NS047101), and General Electric, Investigator Initiated Research Award BOK92325. This material is based upon work supported by the National Science Foundation under grant no. 1430082.

The costs of publication of this article were defrayed in part by the payment of page charges. This article must therefore be hereby marked *advertisement* in accordance with 18 U.S.C. Section 1734 solely to indicate this fact.

Received October 7, 2015; revised December 22, 2015; accepted January 5, 2016; published online June 1, 2016.

Downloaded from clincancerres.aacrjournals.org on October 19, 2021. © 2016 American Association for Cancer Research.

References

1. American Cancer Society. Cancer Facts & Figures 2015.Atlanta, GA: American Cancer Society; 2015.
2. Epstein JI. The lower urinary tract and male genital system. In: Jumar V, Abbas AK, Fausto N, editors. Robbins and Cotran Pathologic Basis of Disease. 7th ed., Philadelphia, PA: Saunders; 2004, p. 1050–8.
3. McNeal JE, Redwine EA, Freiha FS, Stamey TA. Zonal distribution of prostatic adenocarcinoma: correlation with histologic pattern and direction of spread. Am J Surg Pathol 1988;12:897–906.
4. Augustin H, Erbersdobler A, Graefen M, Fernandez S, Palisaar J, Huland H, et al. Biochemical recurrence following radical prostatectomy: A comparison between prostate cancers located in different anatomical zones. Prostate 2003;55:48–54.
5. Carroll PR, Parsons JK, Andriole G, Bahnson RR, Barocas DA, Catalona WJ, et al. Prostate Cancer Early Detection, Version 1.2014: featured updates to the NCCN guidelines. J Natl Compr Cancer Netw 2014;12:1211–9.
6. Johnson LM, Turkbey B, Figg WD, Choyke PL. Multiparametric MRI in prostate cancer management. Nat Rev Clin Oncol 2014;11:346–53.
7. Wu LM, Xu JR, Ye YQ, Lu Q, Hu JN. The clinical value of diffusion-weighted imaging in combination with T2-weighted imaging in diagnosing prostate carcinoma: A systematic review and meta-analysis. Am J Roentgenol 2012;199:103–10.
8. Isebaert S, Van Den Bergh L, Haustermans K, Joniau S, Lerut E, De Wever L, et al. Multiparametric MRI for prostate cancer localization in correlation to whole-mount histopathology. J Magn Reson Imaging 2013; 37:1392–401.
9. Rosenkrantz AB, Taneja SS. Radiologist, be aware: Ten pitfalls that confound the interpretation of multiparametric prostate MRI. Am J Roentgenol 2014;202:109–20.
10. White NS, Leergaard TB, D'Arceuil H, Bjaalie JG, Dale AM. Probing tissue microstructure with restriction spectrum imaging: Histological and theoretical validation.Hum Brain Mapp 2013;34:327–46.
11. Farid N, Almeida-Freitas DB, White NS, McDonald CR, Kuperman JM, Almutairi A a, et al. Combining diffusion and perfusion differentiates tumor from bevacizumab-related imaging abnormality (bria). J Neurooncol 2014;120:539–46.
12. White NS, McDonald CR, Farid N, Kuperman J, Karow D, Schenker-Ahmed NM, et al. Diffusion-weighted imaging in cancer: physical foundations and applications of restriction Spectrum imaging. Cancer Res 2014;74:4638–52.
13. Liss MA, White NS, Parsons JK, Schenker-Ahmed NM, Rakow-Penner R, Kuperman JM, et al. MRI-derived restriction spectrum imaging cellularity index is associated with high grade prostate cancer on radical prostatectomy specimens. Front Oncol 2015;5:1–8.
14. Rakow-Penner RA, White NS, Parsons JK, Choi HW, Liss M a, Kuperman JM, et al. Novel technique for characterizing prostate cancer utilizing MRI restriction spectrum imaging: proof of principle and initial clinical experience with extraprostatic extension. Prostate Cancer Prostatic Dis 2015;18:81–5.
15. Holland D, Kuperman JM, Dale AM. Efficient correction of inhomogeneous static magnetic field-induced distortion in Echo Planar Imaging. Neuroimage 2010;50:175–83.
16. Epstein JI, Allsbrook WCJ, Amin MB, Egevad LL. The 2005 International society of urological pathology (ISUP) consensus conference on Gleason grading of prostatic carcinoma.Am J Surg Pathol 2005;29:1228–42.
17. Epstein JI, Zelefsky MJ, Sjoberg DD, Nelson JB, Egevad L, Magi-Galluzzi C, et al. A contemporary prostate cancer grading system: a validated alternative to the gleason score. Eur Urol 2015:1–8.
18. Gleason DF. Classification of prostatic carcinomas.Cancer Chemother Rep 1966;50:125–8.
19. Bates D, Mächler M, Bolker BM, Walker SC. Fitting linear mixed-effects models using lme4. J Stat Softw 2015;67:1–48.
20. Hothorn T, Bretz F, Westfall P. Simultaneous inference in general parametric models. Biometrical J 2008;50:346–63.
21. R Core Team. R: A language and environment for statistical computing. Vienna, Austria: R Foundation for Statistical Computing; 2015.
22. McCammack KC, Kane CJ, Parsons JK, White NS, Schenker-Ahmed NM, Kuperman JM, et al. *In vivo* prostate cancer detection and grading using Restriction Spectrum Imaging-MRI. Prostate Cancer Prostatic Dis 2016 Jan 12. [Epub ahead of print].
23. Hricak H, Dooms GC, McNeal JE, Mark AS, Marotti M, Avallone A, et al. MR imaging of the prostate gland: normal anatomy. AJR Am J Roentgenol 1987;148:51–8.
24. Myers RP. Structure of the adult prostate from a Clinician's Standpoint.Clin Anat 2000;215:214–5.

Downloaded from clincancerres.aacrjournals.org on October 19, 2021. © 2016 American Association for Cancer Research.

AACR American Association for Cancer Research

Clinical Cancer Research

Voxel Level Radiologic–Pathologic Validation of Restriction Spectrum Imaging Cellularity Index with Gleason Grade in Prostate Cancer

Ghiam Yamin, Natalie M. Schenker-Ahmed, Ahmed Shabaik, et al.

Clin Cancer Res 2016;22:2668-2674.

Updated version	Access the most recent version of this article at: http://clincancerres.aacrjournals.org/content/22/11/2668
Supplementary Material	Access the most recent supplemental material at: http://clincancerres.aacrjournals.org/content/suppl/2016/06/02/22.11.2668.DC1

Cited articles	This article cites 19 articles, 1 of which you can access for free at: http://clincancerres.aacrjournals.org/content/22/11/2668.full#ref-list-1
Citing articles	This article has been cited by 2 HighWire-hosted articles. Access the articles at: http://clincancerres.aacrjournals.org/content/22/11/2668.full#related-urls

E-mail alerts	Sign up to receive free email-alerts related to this article or journal.
Reprints and Subscriptions	To order reprints of this article or to subscribe to the journal, contact the AACR Publications Department at pubs@aacr.org.
Permissions	To request permission to re-use all or part of this article, use this link http://clincancerres.aacrjournals.org/content/22/11/2668. Click on "Request Permissions" which will take you to the Copyright Clearance Center's (CCC) Rightslink site.

Downloaded from clincancerres.aacrjournals.org on October 19, 2021. © 2016 American Association for Cancer Research.